

Dramatic reduction in thermal conductivity by high-density dislocations in SrTiO₃

Jinxue Ding^{1*}, Jiawen Zhang^{2a}, Jinfeng Dong³, Kimitaka Higuchi⁴, Atsutomo Nakamura⁵, Wenjun Lu^{2*}, Bo Sun^{6*}, Xufei Fang¹

¹Institute for Applied Materials, Karlsruhe Institute of Technology, Karlsruhe 76131, Germany

²Department of Mechanical and Energy Engineering, Southern University of Science and Technology, Shenzhen 518055, China

³School of Materials Science and Engineering, Nanyang Technological University, Singapore 639798, Singapore

⁴Institute of Materials and Systems for Sustainability, Nagoya University, Nagoya, Aichi 464-8601, Japan

⁵Graduate School of Engineering Science, Osaka University, Osaka, Toyonaka 560-8531, Japan

⁶Tsinghua SIGS and Guangdong Provincial Key Laboratory of Thermal Management Engineering & Materials, Tsinghua University, Shenzhen 518055, China

^aThese authors contribute equally to this work.

*Corresponding authors:

jinxue.ding@kit.edu (J. D.), luwj@sustech.edu.cn (W. L.), sun.bo@sz.tsinghua.edu.cn (B. S.)

Abstract:

Decreasing thermal conductivity is important for designing efficient thermoelectric devices. Traditional engineering strategies have focused on point defects and interface design. Recently, dislocations as line defects have emerged as a new tool for regulating thermal conductivity. In ceramics-based thermoelectric materials, the key challenge lies in achieving sufficiently high-density dislocations to effectively scatter phonons, as the typical dislocation density in ceramics after bulk deformation is constrained to $\sim 10^{12} \text{ m}^{-2}$. In this work, we adopted the mechanical imprinting method and achieved a dislocation density of $\sim 10^{15} \text{ m}^{-2}$ in single-crystal SrTiO₃, which is known for its room-temperature plasticity and acts as a promising material for thermoelectric applications. Using the time-domain thermoreflectance (TDTR) method, we measured a $\sim 50\%$ reduction in the thermal conductivity over a broad temperature range (80–400 K) with the engineered high-density dislocations. These results suggest that tuning dislocations could offer a new path to minimizing thermal conductivity for engineering thermoelectric materials.

Thermoelectric (TE) materials can convert waste heat into electricity for power generation or, conversely, use electrons as agents to remove heat for cooling applications.^{1,2} This dual functionality makes TE materials valuable in addressing energy challenges. Maintaining a low thermal conductivity is crucial for preserving the temperature gradient, thereby improving the overall conversion efficiency.³ As a result, a key focus in thermoelectrics is to minimize thermal conductivity without compromising the electrical properties.^{4,5} The total thermal conductivity (Λ_{tot}) consists of contributions from both charge carriers (Λ_e) and the lattice (Λ_l). Independently reducing lattice thermal conductivity, Λ_l , is a promising strategy to enhance TE efficiency while maintaining high electrical conductivity.⁶ Up to date, the most widely used strategies for lowering Λ_l include point defect engineering (e.g., doping and alloying)^{7,8} and boundary engineering (e.g., nanostructuring)⁹. Recently, dislocations (one-dimensional or line defects) have emerged as an additional degree of freedom, gaining significant attention as an effective approach to reducing Λ_l .^{10,11}

Dislocation engineering in TE materials is intriguing because it can reduce Λ_l while enhancing electrical¹² and mechanical¹³ properties. In recent years, the role of dislocations in enhancing phonon scattering in ceramics has been revisited with promising proofs of concept. For example, Yin et al.¹⁴ introduced high-density dislocations (up to $\sim 9.1 \times 10^{16} \text{ m}^{-2}$) into BiCuSeO by ultrahigh-pressure sintering to strongly suppress the phonon transport. Abdellaoui et al.¹⁵ studied the characteristics of dislocations in PbTe-based TE material, including their distribution, alignment, and local chemistry, using correlative microscopy techniques. Beyond TE materials, the phenomenon of dislocation-tuned thermal conductivity has also been observed and investigated in semiconductors and other functional ceramics. The anisotropic thermal conductivity caused by oriented dislocations was first predicted by Klemens¹⁶ in the 1950s and more recently experimentally verified by Sun et al.¹⁷ in InN films with oriented threading dislocations. Khafizov et al.¹⁸ highlighted that dislocation loops in nuclear ceramics (CeO_2), formed due to irradiation damage, can significantly affect heat transport.

Thermal conductivity can depend critically on dislocation density.¹⁹ At low dislocation densities, where the spacing between dislocations is much larger than the phonon mean free path (MFP), their influence on phonon transport becomes negligible. In 2020, Johanning et al.²⁰ engineered dislocations into bulk SrTiO_3 by high-temperature plastic deformation. However, no enhanced phonon scattering was observed in the plastically deformed samples due to the low dislocation density ($\sim 10^{12} \text{ m}^{-2}$). Their theoretical model suggested that a significant reduction in thermal conductivity would occur at a dislocation density of around 10^{15} m^{-2} in SrTiO_3 , which was not attainable at that time. To date, various research groups have confirmed that surface dislocations in SrTiO_3 are able to enhance its electrical conductivity.^{21–23} Still, direct

experimental evidence demonstrating a reduction in thermal conductivity due to dislocations in SrTiO₃ remains elusive.

To address this open question, here we adopt undoped single-crystal SrTiO₃ (to avoid the complexity of dopants and grain boundaries), which exhibits exceptional large plasticity even at room temperature²⁴ and is also a well-established material in the TE field^{25,26}, making it an ideal candidate for this research. With the mechanical deformation toolbox developed by the present authors^{13,27,28}, we successfully engineered a high dislocation density (up to $\sim 10^{15} \text{ m}^{-2}$) in the sample by near-surface mechanical deformation. This approach allows to evaluate the thermal conductivity in the dislocation-rich region via the time-domain thermoreflectance (TDTR) method.²⁹⁻³¹

Undoped SrTiO₃ (STO) single crystals with a geometry of $5 \times 5 \times 1 \text{ mm}^3$ from Alineason Materials Technology GmbH (Frankfurt am Main, Germany) were used. Dislocations were engineered in the near-surface region using a mechanically seeded dislocation approach through grinding and polishing (schematic in **Fig. 1a**). Grinding was performed using SiC papers (P2500), applying a force of 15 N and a rotation speed of 150 rpm. The following polishing steps were carried out to ensure a smooth surface. More details on this dislocation seeding approach can be found elsewhere.²⁷ In what follows, pristine STO is referred to as *p*-STO, and STO with surface dislocations as *d*-STO. To observe the dislocation substructure near the surface using the high-voltage transmission electron microscopy (HVTEM), the conventional TEM foil preparation method, which does not introduce additional dislocations into the sample, was adopted. First, two samples with well-preserved surfaces after polishing were prepared and bonded with epoxy to form a stable interface. Then, while ensuring the integrity of the interface, normal mechanical polishing, dimpling, and ion milling with Ar ions were performed from the side to produce a thin film for TEM observation that retained the original surface structure. The observation images were obtained using an ultra-high voltage electron microscope (JEOL JEM-1000K RS, 1000 keV) in bright-field mode.

For local dislocation structure characterization and 3D reconstruction of the dislocations, additional TEM thin lamellae with approximately 50 nm in thickness were prepared using a focused ion beam (FIB) system (Helios Nanolab 600i, FEI, Hillsboro, USA). These TEM samples were characterized using a field emission TEM (Talos F200X G2) operating at 200 kV. For annular bright-field (ABF)-scanning TEM (STEM) imaging a probe semi-convergence angle of 17 mrad and inner and outer semi-collection angles ranging from 13 to 21 mrad were utilized. The microstructures of STO, including dislocations, were analyzed using a 200 kV TEM in STEM mode. Tilt-series of ABF-STEM images were acquired using Xplore3D software (FEI Company), with dynamic focusing incorporated during image acquisition. A high-angle tomography holder (Model 2020, Fischione, USA) was used for tilt-series acquisition, with a

maximum tilt angle of 60°, which was necessary to observe the same set of dislocations in all tilt-series images. During these experiments, the [001] direction of the lamella specimens was aligned with the tilt axis of the specimen holder. The tilt-series images were then aligned, and 3D datasets were reconstructed using Inspect3DIII software (Thermo Fisher Scientific Inc.), employing the simultaneous iterative reconstruction technique (SIRT) for 40 iterations. All tilt-series STEM images were utilized for the 3D reconstruction, and the final 3D models were visualized using Amira-Avizo™ software.

To measure the through-plane thermal conductivity in the near-surface region, an aluminum (Al) layer with a thickness of ~70 nm was deposited on the surface of samples by e-beam evaporation. The TDTR method was carried out using the 5x objective lens (1/e² radius of 12 μm) with a modulation frequency (f) of 10 MHz. Thermal transport is modeled as the propagation of thermal waves in layered structure at a given modulation frequency, $f = 10$ MHz in this case. This results in a thermal penetration depth d , which is given by the equation: $d = \sqrt{\Lambda/\pi f C}$, with Λ and C being the thermal conductivity and volumetric specific heat of the sample, respectively. The penetration depth d is calculated to be less than 1 μm, to make sure we measure dislocation-rich region.

The HVTEM image in **Fig. 1b** revealed that the cross-section of the deformed surface layer (up to a depth of ~3 μm) is enriched with high-density dislocations. In contrast, bright-field TEM (BF-TEM) image for p -STO shows no visible dislocations (**Fig. S1**). Particularly, no subgrain boundaries or amorphous phases were detected in the highly deformed region in d -STO, according to the selected area electron diffraction (SAED) pattern (**Fig. S1**). The dislocation density is determined by the line intercept method using TEM images³² (**Fig. S1c** and **Fig. 1b**), reaching up to ~10¹⁵ m⁻². As the grinding particles have a limited range of stress field exerted on the sample surface, the dislocation density drops sharply beyond ~3 μm in depth. Beyond this deformation layer (bottom of **Fig. 1b**), the sample can be regarded as pristine STO. The pristine sample has a grown-in dislocation density of 10¹⁰ m⁻², as reported in pervious studies^{33,34}. The limited dislocation region in the depth direction merits the use of TDTR measurement, which can achieve a penetration depth less than 1 μm to focus on the impact of dislocations.

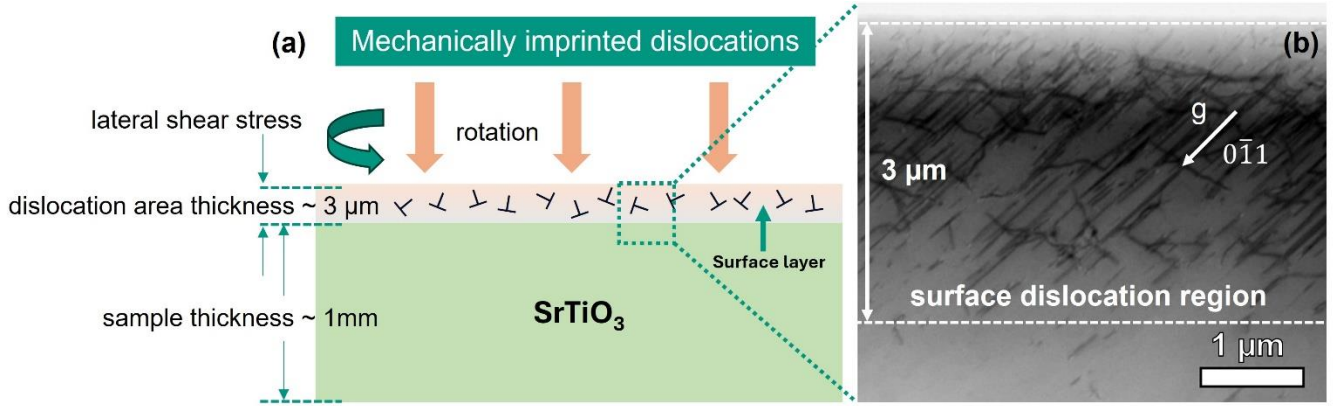


FIG. 1. (a) Schematic illustration of the mechanical imprinting method; (b) cross-sectional HVTEM image of near-surface region of the *d*-STO sample, as indicated by green rectangle in (a). The upper dashed line in (b) indicates the sample surface.

The temperature-dependent thermal conductivity demonstrates a clear difference (**Fig. 2**) for both *p*-STO and *d*-STO samples. For benchmarking purpose, in *p*-STO with a dislocation density of $\sim 10^{10} \text{ m}^{-2}$ (almost dislocation-free for the laser spot area), the TDTR results are in excellent agreement with those reported by Yu et al.³⁵, measured using a 3ω method. The *p*-STO sample exhibits a typical temperature-dependent behavior of thermal conductivity. As the temperature increases within the measurement range, thermal conductivity initially rises due to the enhanced phonon population and the corresponding increase in heat-carrying phonons. As the temperature continues to rise, phonon-phonon scattering intensifies, leading to a peak in thermal conductivity, after which it decreases. For *d*-STO, $\sim 50\%$ to $\sim 60\%$ decrease in thermal conductivity is observed over the wide temperature range (80–400K). The distinct difference between the *p*-STO and *d*-STO samples underscores the significant role of dislocations in scattering phonons, effectively suppressing temperature-dependent behaviors and reducing thermal conductivity. As presented in **Fig. S2**, the *p*-STO sample displays a typical TDTR signal with one picoacoustic peak, indicating that the thermal stress wave is reflected at the interface between the Al film and STO. In contrast, the *d*-STO sample shows a second peak, suggesting the presence of acoustic wave reflections caused by dislocations.

For both *p*-STO and *d*-STO samples in the measured temperature range, heat transport is predominantly governed by phonon transport and the contribution of electronic thermal conductivity is negligible. The measured thermal conductivity can be considered as Λ_l . The theoretical minimum of Λ_l for highly disordered crystals can be calculated using the Cahill-Pohl model³⁶, which is expressed as follows:

$$\Lambda_{l,min} = \left(\frac{\pi}{6}\right)^{\frac{1}{3}} k_B n^{\frac{2}{3}} \sum_i v_i \left(\frac{T}{\theta_i}\right)^2 \int_0^{\frac{\theta_i}{T}} \frac{x^3 e^x}{(e^x - 1)^2} dx \quad (1)$$

where $x = \frac{\hbar\omega}{k_B T}$ with ω being the phonon angular frequency, k_B is the Boltzmann constant, v_i the sound velocity, n is the number density of atoms, and θ_i is the Debye temperature. The calculated $\Lambda_{l,min}$ ranges from 1 to 2 $\text{Wm}^{-1}\text{K}^{-1}$, as shown in **Fig. S3**. It suggests that the introduced high-density dislocations are not sufficiently disordered to achieve the lower limit of Λ_l , which is reasonable that the theoretical $\Lambda_{l,min}$ is achieved with a phonon MFP down to the distance of the nearest atoms.

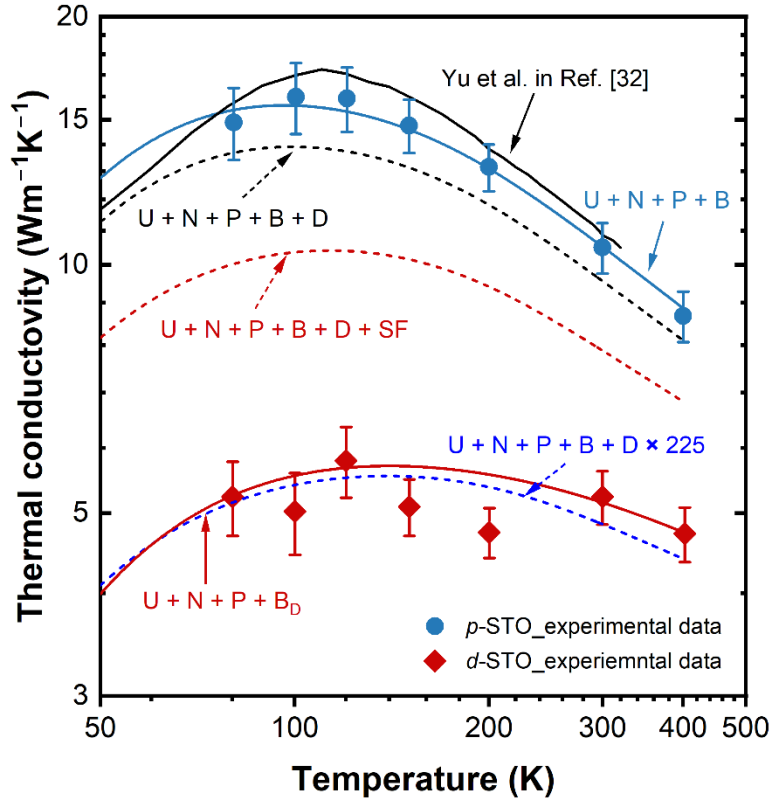


FIG. 2. The measured temperature-dependent thermal conductivity by TDTR and analysis of phonon transport process using modified Debye-Callaway model. Phonon-dislocation scattering is evaluated by treating dislocations as line defects (D) and/or 2D stacking faults (SF), following the Klemens model. Note: U for Umklapp phonon-phonon scattering, N for normal phonon-phonon scattering, P for point defect scattering, B for boundary scattering, D for dislocation scattering, SF for stacking faults scattering, B_D for dislocation-induced boundary scattering.

The experimental data indicate that dislocations significantly suppress Λ_l , especially at low temperatures. To gain deeper insights into the role of dislocations, we employ the modified Debye-Callaway model to

interpret the measured data. Then, Λ_l can be calculated by considering the contribution from individual acoustic phonon branches (one longitudinal and two transverse acoustic branches), as expressed by the following equations^{37,38}:

$$\Lambda_l = \sum_i \Lambda_{l,i} = \sum_i \frac{k_B}{6\pi^2 v_i} \left(\frac{k_B T}{\hbar} \right)^3 \left(I_{i1} + \frac{I_{i2}^2}{I_{i3}} \right) \quad (2)$$

The details for a specific phonon branch (I_{i1}, I_{i2}, I_{i3}) are presented in the Supplementary Materials. The combined relaxation time for phonons (τ_i^C) can be written as follows according to Matthiessen's rule, including normal phonon-phonon scattering (N), Umklapp phonon-phonon scattering (U), point defect scattering (P), boundary scattering (B), dislocation scattering (D), etc., as in:

$$\frac{1}{\tau_i^C} = \frac{1}{\tau_i^N} + \frac{1}{\tau_i^U} + \frac{1}{\tau_i^P} + \frac{1}{\tau_i^B} + \frac{1}{\tau_i^D} + \dots \quad (3)$$

It may seem odd at first sight for including point defect scattering and boundary scattering for single-crystal *p*-STO. According to the model (see Supplementary Materials), these two mechanisms should be considered even for the undoped single-crystal sample. When the contribution of boundary scattering is ignored, Λ_l can be very high at low temperatures, as shown in **Fig. S3**. Considering that STO goes through a phase transition from cubic to tetragonal around 105 K³⁹, the results suggest that domain structures^{40,41} occurred near the phase transition may behave like 2D boundaries and can strongly scatter phonons. The point defect scattering parameter Γ and boundary scattering characteristic dimension L_c are fitted based on the experimental data of *p*-STO, yielding values of $\Gamma = 0.206$ and $L_c = 458$ nm, which are then applied to *d*-STO. The point defect scattering can be explained by the well-known existence of oxygen vacancies⁴², locally atomic-scale structures caused by off-centering atoms^{43,44}, and other impurity ions introduced during the growth of single-crystal STO.

For *d*-STO, dislocation scattering is specifically included based on the Klemens model¹⁶ (see Supplementary Materials). However, the Klemens model predicts only a small reduction in thermal conductivity, as indicated by the black dashed line in **Fig. 2**. Note that back in 1959, significant discrepancies were observed between the experimental data and values predicted by Klemens model in LiF.⁴⁵ Carruthers⁴⁶ later found that the Klemens model underestimated the influence of strain fields from edge-type dislocations and proposed the later known Carruthers model. However, for screw-type dislocations, Carruthers model concurred with the predictions made by Klemens. We note that the Carruthers model may not apply to the experimental data here, as the surface dislocations mechanically introduced are primarily screw-type dislocations, with very few edge-type dislocation segments located at the end of the screw dislocation lines²⁷. It is worth mentioning that Khafizov et al.¹⁸ recently proposed that treating dislocation loops as faulted dislocations, rather than line dislocations, has a significant impact

on phonon scattering and provides a better fit to the experimental data. As SrTiO₃ has been well-documented by numerous TEM studies to show that the dislocations dissociate around room temperature^{47,48}, therefore, by further including stacking fault (SF) scattering, a relatively large decrease in thermal conductivity can be predicted (red dashed line in **Fig. 2**), although it may still not reach the levels observed in the measured data. The model provides a satisfying prediction of the thermal behavior of *p*-STO, successfully capturing the peak temperature where the thermal conductivity reaches its maximum. However, the existing models for dislocations significantly underestimate their impact on phonon scattering, even when dislocations are treated as 2D stacking faults. It should be noted that this model does not account for the potential reduction in phonon velocity caused by stress-induced lattice softening, which may explain part of the discrepancy but not the large deviation observed. To fit the experimental data, the dislocation scattering rate from Klemens model needs to be magnified by a factor of 225, indicated by the blue dashed line in **Fig. 2**. The physical justification for the choice of 225 remains elusive, therefore, we discuss in what follows another possibility.

The existing models for dislocation scattering are unable to satisfactorily capture the reduction in thermal conductivity induced by the high-density dislocations. This discrepancy may arise since these models did not consider the complex dislocation structures, as visualized by the ABF-STEM observations (**Fig. 3**). The classic models assume dislocations as weak and isolated phonon scattering centers, more valid for low-density dislocations ($10^{12-13} \text{ m}^{-2}$). With dislocation density increasing up to $\sim 10^{15} \text{ m}^{-2}$, they are no longer isolated line defects but form a complex spatial network, as depicted in **Fig. 3f** for the reconstructed 3D tomography. Five snapshots from the ABF-STEM video (**Video S1**), captured while rotating the sample, are displayed in **Figs. 3a-3e**, respectively. These images reveal that, in addition to typical 1D dislocations lines, other defects, e.g., dislocation loops, stacking faults, dislocation dipoles, all arranged in a sophisticated 3D manner, are also present. These complexity of dislocation structures and their interaction (strain field) with each other shall be considered in the future model to quantitatively describe the dislocation-induced thermal transport behavior.⁴⁹

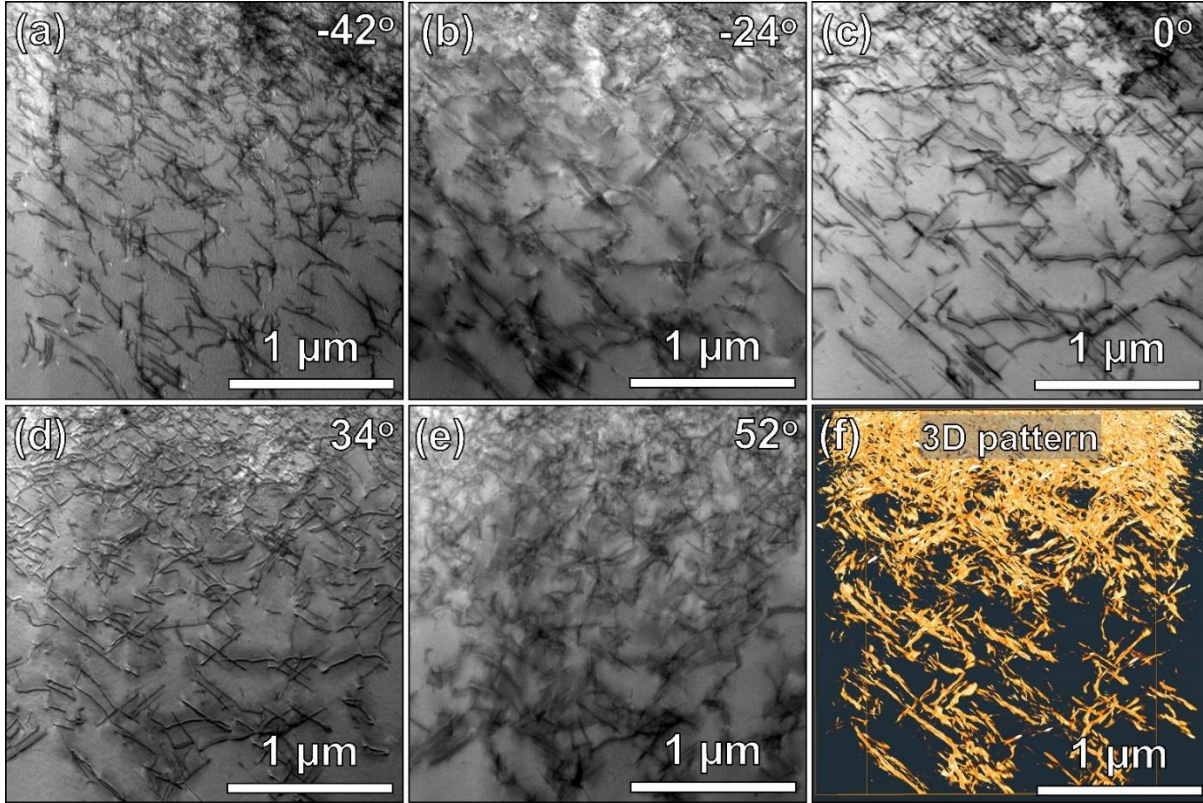


FIG. 3. 3D reconstruction of *d*-STO lamella with mechanically seeded dislocations. (a-e) A series of ABF-STEM images tilted along $\langle 100 \rangle$ axis from -42° to 52° ; (f) the corresponding 3D image showing the dislocation networks.

Moreover, as TEM is primarily a 2D visualization tool, the determination of dislocation density and the characterization of complex dislocation geometries using TEM alone may not be sufficient. For high-density dislocations, caution must be taken for the determination of their density and spatial arrangement since dislocations may overlap or form entangled networks (**Fig. 3**). Furthermore, the high-density dislocations in STO may interact with domain structures at temperatures below 105 K, leading to the formation of more complex structures. Thus, more advanced correlative techniques to comprehensively determine dislocation structures is needed for future studies. For example, dark-field X-ray microscopy can provide both high spatial resolution and the ability to directly probe the dislocation structures in 3D manner, yet its spatial resolution is limited to ~ 100 nm.⁵⁰ In addition, the intertwined dislocations, their overlapped strain fields, and their interactions with domain structures may form a quasi-periodic boundary, which can strongly interact with phonons, particularly those with long wavelengths, similar to the impact by boundaries or interfaces. In this case, by treating the dislocation-phonon scattering as dislocation-induced boundary scattering (B_D), the experimental data can be well captured by adjusting the

characteristic dimension parameter L_c to be 100 nm (larger than the average dislocation spacing in the current case), as shown by the red solid line in **Fig. 2**. This characteristic length L_c should be closely related to the density and arrangement of dislocations, and potentially other physical properties (e.g., elasticity, crystal structure, etc.) of the material, which can affect dislocation interactions. It could be valuable to link L_c to other parameters in the future work, as this may provide insights into the impact of dislocations on phonon scattering, particularly in the high-density regimes.

Mechanically seeded high-density dislocations, up to $\sim 10^{15} \text{ m}^{-2}$ as visualized by transmission electron microscopy, in undoped single-crystal SrTiO_3 is experimentally observed to significantly reduce thermal conductivity by up to $\sim 60\%$. Much more pronounced impact of dislocations in reducing thermal conductivity is observed than previous model prediction, especially at low temperatures. This discrepancy is likely caused by the complex dislocation structures and spatial distribution, which were not accounted for in the past models. The interactions between dislocations and phonons require further exploration to gain a deeper understanding of how the dislocation approach can be optimized to tune thermal conductivity. It is expected that this approach of mechanically seeding dislocations can be extended to e.g., Nb-doped SrTiO_3 , which has good electrical conductivity for promising thermoelectric performance, provided that the thermal conductivity can be significantly reduced by high density dislocations.

Acknowledgement

J. Ding and X. Fang thank for the final support by ERC project MECERDIS (No. 101076167). Views and opinions expressed are however those of the authors only and do not necessarily reflect those of the European Union or the European Research Council. Neither the European Union nor the granting authority can be held responsible for them. W. Lu acknowledges the support by Shenzhen Science and Technology Program (grant no. JCYJ20230807093416034) and the Open Fund of the Microscopy Science and Technology-Songshan Lake Science City (grant no. 202401204). The authors acknowledge the use of the facilities at the Southern University of Science and Technology Core Research Facility. B. Sun would like to thank the National Science Foundation of China (Nos. 52161145502 and 12004211), the Shenzhen Science and Technology Program (grant no. RCYX20200714114643187 and WDZC20200821100123001), and the Guangdong Special Support Program (No. 2023TQ07A273). We thank Dr. L. Porz from Illutherm GmbH, Prof. G. Snyder from Northwestern University, Prof. J. Rödel from TU Darmstadt, Prof. M. Yoshiya and W. Sekimoto from Osaka University for the initial discussions. The authors also thank S. Stich and H. Song for sample preparation.

Reference

- ¹ J. He, and T.M. Tritt, “Advances in thermoelectric materials research: Looking back and moving forward,” *Science* **357**(6358), eaak9997 (2017).
- ² X.-L. Shi, J. Zou, and Z.-G. Chen, “Advanced Thermoelectric Design: From Materials and Structures to Devices,” *Chem. Rev.* **120**(15), 7399–7515 (2020).
- ³ M. Hamid Elsheikh, D.A. Shnawah, M.F.M. Sabri, S.B.M. Said, M. Haji Hassan, M.B. Ali Bashir, and M. Mohamad, “A review on thermoelectric renewable energy: Principle parameters that affect their performance,” *Renew. Sustain. Energy Rev.* **30**, 337–355 (2014).
- ⁴ Z. Chen, X. Zhang, and Y. Pei, “Manipulation of Phonon Transport in Thermoelectrics,” *Adv. Mater.* **30**(17), 1705617 (2018).
- ⁵ P. Wei, C. Liao, H. Wu, D. Yang, J. He, G.V. Biesold-McGee, S. Liang, W. Yen, X. Tang, J. Yeh, Z. Lin, and J. He, “Thermodynamic Routes to Ultralow Thermal Conductivity and High Thermoelectric Performance,” *Adv. Mater.* **32**(12), 1906457 (2020).
- ⁶ C.-D. Zhou, B. Liang, W.-J. Huang, J.-G. Noudem, X.-J. Tan, and J. Jiang, “Phonon engineering significantly reducing thermal conductivity of thermoelectric materials: a review,” *Rare Met.* **42**(9), 2825–2839 (2023).
- ⁷ T. Xing, C. Zhu, Q. Song, H. Huang, J. Xiao, D. Ren, M. Shi, P. Qiu, X. Shi, F. Xu, and L. Chen, “Ultralow Lattice Thermal Conductivity and Superhigh Thermoelectric Figure-of-Merit in (Mg, Bi) Co-Doped GeTe,” *Adv. Mater.* **33**(17), 2008773 (2021).
- ⁸ H. Wang, J. Wang, X. Cao, and G.J. Snyder, “Thermoelectric alloys between PbSe and PbS with effective thermal conductivity reduction and high figure of merit,” *J. Mater. Chem. A* **2**(9), 3169 (2014).
- ⁹ M.S. Toprak, C. Stiewe, D. Platzek, S. Williams, L. Bertini, E. Müller, C. Gatti, Y. Zhang, M. Rowe, and M. Muhammed, “The Impact of Nanostructuring on the Thermal Conductivity of Thermoelectric CoSb₃,” *Adv. Funct. Mater.* **14**(12), 1189–1196 (2004).
- ¹⁰ Z. Chen, B. Ge, W. Li, S. Lin, J. Shen, Y. Chang, R. Hanus, G.J. Snyder, and Y. Pei, “Vacancy-induced dislocations within grains for high-performance PbSe thermoelectrics,” *Nat. Commun.* **8**(1), 13828 (2017).
- ¹¹ Y. Jiang, J. Dong, H.-L. Zhuang, J. Yu, B. Su, H. Li, J. Pei, F.-H. Sun, M. Zhou, H. Hu, J.-W. Li, Z. Han, B.-P. Zhang, T. Mori, and J.-F. Li, “Evolution of defect structures leading to high ZT in GeTe-based thermoelectric materials,” *Nat. Commun.* **13**(1), 6087 (2022).
- ¹² C. Rodenbücher, D. Wrana, T. Gensch, F. Krok, C. Korte, and K. Szot, “The Electronic Properties of Extended Defects in SrTiO₃—A Case Study of a Real Bicrystal Boundary,” *Crystals* **10**(8), 665 (2020).
- ¹³ X. Fang, A. Nakamura, and J. Rödel, “Deform to perform: Dislocation-tuned properties of ceramics,” *Am. Ceram. Soc. Bull.* **102**, 24–29 (2023).
- ¹⁴ Z. Yin, H. Zhang, Y. Wang, Y. Wu, Y. Xing, X. Wang, X. Fang, Y. Yu, and X. Guo, “Ultrahigh-Pressure Structural Modification in BiCuSeO Ceramics: Dense Dislocations and Exceptional Thermoelectric Performance,” *Adv. Energy Mater.*, 2403174 (2024).
- ¹⁵ L. Abdellaoui, Z. Chen, Y. Yu, T. Luo, R. Hanus, T. Schwarz, R. Bueno Villoro, O. Cojocar-Miréidin, G.J. Snyder, D. Raabe, Y. Pei, C. Scheu, and S. Zhang, “Parallel Dislocation Networks and Cottrell Atmospheres Reduce Thermal Conductivity of PbTe Thermoelectrics,” *Adv. Funct. Mater.* **31**(20), 2101214 (2021).
- ¹⁶ P.G. Klemens, “The Scattering of Low-Frequency Lattice Waves by Static Imperfections,” *Proc. Phys. Soc. Sect. A* **68**(12), 1113–1128 (1955).
- ¹⁷ B. Sun, G. Haunschild, C. Polanco, J. Ju, L. Lindsay, G. Koblmüller, and Y.K. Koh, “Dislocation-induced thermal transport anisotropy in single-crystal group-III nitride films,” *Nat. Mater.* **18**(2), 136–140 (2019).
- ¹⁸ M. Khafizov, J. Pakarinen, L. He, and D.H. Hurley, “Impact of irradiation induced dislocation loops on thermal conductivity in ceramics,” *J. Am. Ceram. Soc.* **102**(12), 7533–7542 (2019).
- ¹⁹ C. Mion, J.F. Muth, E.A. Preble, and D. Hanser, “Accurate dependence of gallium nitride thermal conductivity on dislocation density,” *Appl. Phys. Lett.* **89**(9), 092123 (2006).

- ²⁰ M. Johanning, L. Porz, J. Dong, A. Nakamura, J.-F. Li, and J. Rödel, "Influence of dislocations on thermal conductivity of strontium titanate," *Appl. Phys. Lett.* **117**(2), 021902 (2020).
- ²¹ K. Szot, C. Rodenbücher, G. Bihlmayer, W. Speier, R. Ishikawa, N. Shibata, and Y. Ikuhara, "Influence of Dislocations in Transition Metal Oxides on Selected Physical and Chemical Properties," *Crystals* **8**(6), 241 (2018).
- ²² L. Porz, T. Frömling, A. Nakamura, N. Li, R. Maruyama, K. Matsunaga, P. Gao, H. Simons, C. Dietz, M. Rohnke, J. Janek, and J. Rödel, "Conceptual Framework for Dislocation-Modified Conductivity in Oxide Ceramics Deconvoluting Mesoscopic Structure, Core, and Space Charge Exemplified for SrTiO₃," *ACS Nano* **15**(6), 9355–9367 (2021).
- ²³ K.K. Adepalli, J. Yang, J. Maier, H.L. Tuller, and B. Yildiz, "Tunable Oxygen Diffusion and Electronic Conduction in SrTiO₃ by Dislocation-Induced Space Charge Fields," *Adv. Funct. Mater.* **27**(22), 1700243 (2017).
- ²⁴ D. Brunner, S. Taeri-Baghadrani, W. Sigle, and M. Rühle, "Surprising Results of a Study on the Plasticity in Strontium Titanate," *J. Am. Ceram. Soc.* **84**(5), 1161–1163 (2001).
- ²⁵ M.T. Dylla, J.J. Kuo, I. Witting, and G.J. Snyder, "Grain Boundary Engineering Nanostructured SrTiO₃ for Thermoelectric Applications," *Adv. Mater. Interfaces* **6**(15), 1900222 (2019).
- ²⁶ X.-L. Shi, H. Wu, Q. Liu, W. Zhou, S. Lu, Z. Shao, M. Dargusch, and Z.-G. Chen, "SrTiO₃-based thermoelectrics: Progress and challenges," *Nano Energy* **78**, 105195 (2020).
- ²⁷ X. Fang, W. Lu, J. Zhang, C. Minnert, J. Hou, S. Bruns, U. Kunz, A. Nakamura, K. Durst, and J. Rödel, "Harvesting room-temperature plasticity in ceramics by mechanically seeded dislocations," *Mater. Today* **82**, 81–91 (2024).
- ²⁸ X. Fang, O. Preuß, P. Breckner, J. Zhang, and W. Lu, "Engineering dislocation-rich plastic zones in ceramics via room-temperature scratching," *J. Am. Ceram. Soc.* **106**(8), 4540–4545 (2023).
- ²⁹ D.G. Cahill, "Analysis of heat flow in layered structures for time-domain thermoreflectance," *Rev. Sci. Instrum.* **75**(12), 5119–5122 (2004).
- ³⁰ B. Sun, and Y.K. Koh, "Understanding and eliminating artifact signals from diffusely scattered pump beam in measurements of rough samples by time-domain thermoreflectance (TDTR)," *Rev. Sci. Instrum.* **87**(6), 064901 (2016).
- ³¹ Y. Liu, Q. Li, F. Liu, X. Wang, and B. Sun, "Boundary conditions dictate frequency dependence of thermal conductivity in silicon," (2024).
- ³² Y. Meng, X. Ju, and X. Yang, "The measurement of the dislocation density using TEM," *Mater. Charact.* **175**, 111065 (2021).
- ³³ X. Fang, K. Ding, C. Minnert, A. Nakamura, and K. Durst, "Dislocation-based crack initiation and propagation in single-crystal SrTiO₃," *J. Mater. Sci.* **56**(9), 5479–5492 (2021).
- ³⁴ X. Fang, H. Bishara, K. Ding, H. Tsybenko, L. Porz, M. Höfling, E. Bruder, Y. Li, G. Dehm, and K. Durst, "Nanoindentation pop-in in oxides at room temperature: Dislocation activation or crack formation?," *J. Am. Ceram. Soc.* **104**(9), 4728–4741 (2021).
- ³⁵ C. Yu, M.L. Scullin, M. Huijben, R. Ramesh, and A. Majumdar, "Thermal conductivity reduction in oxygen-deficient strontium titanates," *Appl. Phys. Lett.* **92**(19), 191911 (2008).
- ³⁶ D.G. Cahill, S.K. Watson, and R.O. Pohl, "Lower limit to the thermal conductivity of disordered crystals," *Phys. Rev. B* **46**(10), 6131–6140 (1992).
- ³⁷ D.T. Morelli, J.P. Heremans, and G.A. Slack, "Estimation of the isotope effect on the lattice thermal conductivity of group IV and group III-V semiconductors," *Phys. Rev. B* **66**(19), 195304 (2002).
- ³⁸ C. Zhang, F. Liu, S. Guo, Y. Zhang, X. Xu, K.A. Mkhoyan, B. Jalan, and X. Wang, "Temperature-dependent thermal conductivity of MBE-grown epitaxial SrSnO₃ films," *Appl. Phys. Lett.* **123**(4), 042201 (2023).
- ³⁹ T. Riste, E.J. Samuelsen, K. Otnes, and J. Feder, "Critical behaviour of SrTiO₃ near the 105°K phase transition," *Solid State Commun.* **9**(17), 1455–1458 (1971).
- ⁴⁰ R.A. Cowley, "Lattice Dynamics and Phase Transitions of Strontium Titanate," *Phys. Rev.* **134**(4A), A981–A997 (1964).
- ⁴¹ Y. Frenkel, N. Haham, Y. Shperber, C. Bell, Y. Xie, Z. Chen, Y. Hikita, H.Y. Hwang, E.K.H. Salje, and B. Kalisky, "Imaging and tuning polarity at SrTiO₃ domain walls," *Nat. Mater.* **16**(12), 1203–1208 (2017).

- ⁴² R.A. De Souza, "Oxygen Diffusion in SrTiO₃ and Related Perovskite Oxides," *Adv. Funct. Mater.* **25**(40), 6326–6342 (2015).
- ⁴³ J. Dong, L. Hu, J. Liu, Y. Liu, Y. Jiang, Z. Yu, X.Y. Tan, A. Suwardi, Q. Zheng, Q. Li, J. Li, V.P. Dravid, Q. Yan, and M.G. Kanatzidis, "Off-Centering of Ge Atoms in GeBi₂Te₄ and Impact on Thermoelectric Performance," *Adv. Funct. Mater.* **34**(18), 2314499 (2024).
- ⁴⁴ J. Dong, Y. Jiang, Y. Sun, J. Liu, J. Pei, W. Li, X.Y. Tan, L. Hu, N. Jia, B. Xu, Q. Li, J.-F. Li, Q. Yan, and M.G. Kanatzidis, "Discordant Distortion in Cubic GeMnTe₂ and High Thermoelectric Properties of GeMnTe₂ - x %SbTe," *J. Am. Chem. Soc.* **145**(3), 1988–1996 (2023).
- ⁴⁵ R.L. Sproull, M. Moss, and H. Weinstock, "Effect of Dislocations on the Thermal Conductivity of Lithium Fluoride," *J. Appl. Phys.* **30**(3), 334–337 (1959).
- ⁴⁶ P. Carruthers, "Scattering of Phonons by Elastic Strain Fields and the Thermal Resistance of Dislocations," *Phys. Rev.* **114**(4), 995–1001 (1959).
- ⁴⁷ Z. Zhang, W. Sigle, W. Kurtz, and M. Rühle, "Electronic and atomic structure of a dissociated dislocation in SrTiO₃," *Phys. Rev. B* **66**(21), 214112 (2002).
- ⁴⁸ L. Jin, X. Guo, and C.L. Jia, "TEM study of <110>-type 35.26° dislocations specially induced by polishing of SrTiO₃ single crystals," *Ultramicroscopy* **134**, 77–85 (2013).
- ⁴⁹ Y. Cheng, M. Nomura, S. Volz, and S. Xiong, "Phonon–dislocation interaction and its impact on thermal conductivity," *J. Appl. Phys.* **130**(4), 040902 (2021).
- ⁵⁰ C. Yildirim, H.F. Poulsen, G. Winther, C. Detlefs, P.H. Huang, and L.E. Dresselhaus-Marais, "Extensive 3D mapping of dislocation structures in bulk aluminum," *Sci. Rep.* **13**(1), 3834 (2023).

Supplementary Material

Dramatic reduction in thermal conductivity by high-density dislocations in SrTiO₃

Jinxue Ding^{1*a}, Jiawen Zhang^{2a}, Jinfeng Dong³, Kimitaka Higuchi⁴, Atsutomo Nakamura⁵, Wenjun Lu^{2*}, Bo Sun^{6*}, Xufei Fang¹

¹Institute for Applied Materials, Karlsruhe Institute of Technology, Karlsruhe 76131, Germany

²Department of Mechanical and Energy Engineering, Southern University of Science and Technology, Shenzhen 518055, China

³School of Materials Science and Engineering, Nanyang Technological University, Singapore 639798, Singapore

⁴Institute of Materials and Systems for Sustainability, Nagoya University, Nagoya, Aichi 464-8601, Japan

⁵Graduate School of Engineering Science, Osaka University, Osaka, Toyonaka 560-8531, Japan

⁶Tsinghua SIGS and Guangdong Provincial Key Laboratory of Thermal Management Engineering & Materials, Tsinghua University, Shenzhen 518055, China

^aThese authors contribute equally to this work.

*Corresponding authors:

jinxue.ding@kit.edu (J. D.), luwj@sustech.edu.cn (W. L.), sun.bo@sz.tsinghua.edu.cn (B. S.)

1. Structure of surface dislocations

Cross-sectional TEM lamella samples are prepared from bulk samples in the near-surface region. The bright-field TEM (BF-TEM) images visualize the morphology and distribution of surface dislocations (see **Fig. S1**). **Fig. S1a** shows that the *p*-STO sample is free of dislocations, and the selected area electron diffraction (SAED) pattern in the inset further confirms that the sample is in single-crystal for with a (001) orientation. BF-TEM image of *d*-STO (**Fig. S1b**) reveals the formation of a large number of dislocations in the near-surface region. The corresponding SAED pattern confirms that the sample remains in single-crystal from after high-density dislocations are introduced, with no formation of amorphous phases. The low-angle annular dark field-scanning transmission electron microscopy (LAADF-STEM) image (**Fig. S1c**) shows that most of the dislocations are generated and align parallel to the {110} planes. The average spacing between two adjacent dislocations is examined to be ~30 nm from the LAADF-STEM image (see also **Fig. 3** in main text), and the dislocation density is calculated to be around 10^{15} m^{-2} according to the dislocation spacing.

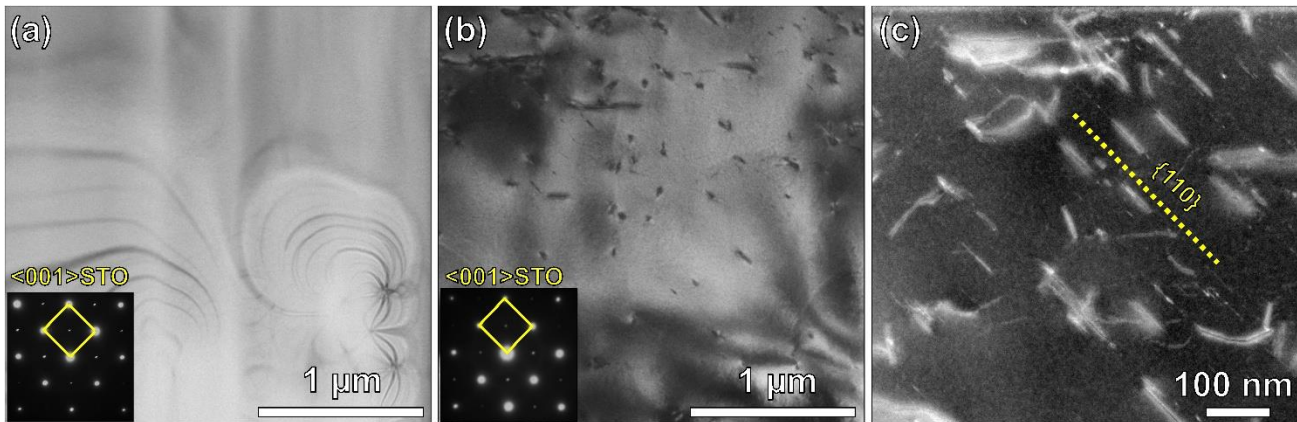


FIG. S1. Bright-field TEM images for (a) *p*-STO and (b) *d*-STO; (c) A low-angle annular dark field-scanning transmission electron microscopy (LAADF-STEM) image for *d*-STO.

2. Time-domain thermoreflectance (TDTR) measurement

For the *p*-STO sample, the in-phase signal (**Fig. S2a1**) is a typical TDTR signal with one picoacoustic peak, showing the thermal stress wave is reflected at the interface between Al and STO. For *d*-STO with surface dislocation, the measured in-phase signal presented in **Fig. S2b1** illustrates that the picoacoustic peak is stronger than the one in *p*-STO, and the second peak can be recognized, indicating that there are multiple acoustic waves reflection, which suggests high density of defects exist near the interface. The fitting curve of TDTR ratio signal (**Fig. S2b1** and **Fig. S2b2**) shows an excellent agreement with the

measured data. The fitting curve also identify with the measured signal, but the absolute value ratio is 2 at 100 ps for d -STO, lower than that of p -STO, indicating the dramatic decrease in thermal conductivity.

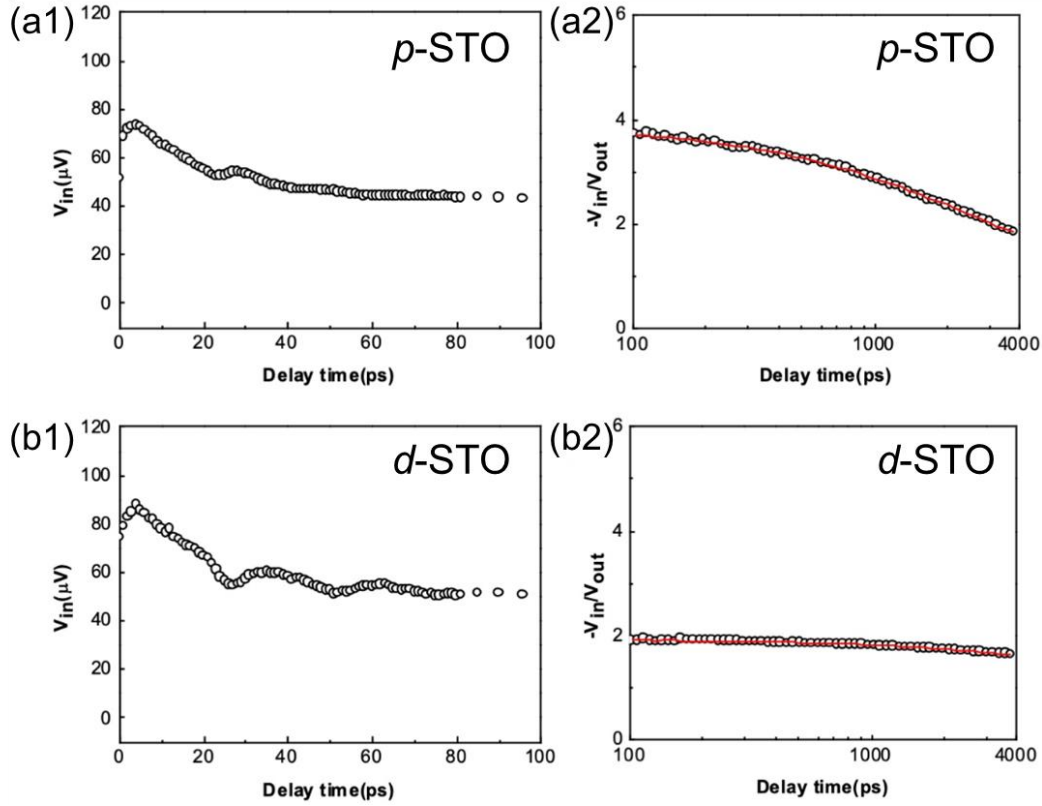


FIG. S2. TDTR signals for both p -STO and d -STO. (a1) V_{in} and (a2) $-V_{in}/V_{out}$ signal of p -STO; (b1) V_{in} and (b2) $-V_{in}/V_{out}$ signal of d -STO.

3. Calculations of lattice thermal conductivity using the modified Debye-Callaway model

The lattice thermal conductivity is calculated according to the modified Debye-Callaway model, as expressed as^{1,2}:

$$\Lambda_l = \sum_i \Lambda_{l,i} = \sum_i \frac{k_B}{6\pi^2 v_i} \left(\frac{k_B T}{\hbar} \right)^3 \left(I_{i1} + \frac{I_{i2}^2}{I_{i3}} \right) \quad (S1)$$

$\Lambda_{l,i}$ is the contribution from individual acoustic phonon branches to lattice thermal conductivity, including one longitudinal and two transverse acoustic branches.

For a specific phonon branch, the integrals I_{i1} , I_{i2} , I_{i3} are defined as follows:

$$I_{i1} = \int_0^{\frac{\theta_{D,i}}{T}} x^4 \frac{e^x}{(e^x - 1)^2} \tau_i^C dx \quad (S2)$$

$$I_{i2} = \int_0^{\frac{\theta_{D,i}}{T}} x^4 \frac{e^x}{(e^x - 1)^2} \frac{\tau_i^C}{\tau_i^N} dx \quad (S3)$$

$$I_{i3} = \int_0^{\frac{\theta_{D,i}}{T}} x^4 \frac{e^x}{(e^x - 1)^2} \frac{\tau_i^C}{\tau_i^N \tau_i^R} dx \quad (S4)$$

where $x = \frac{\hbar\omega}{k_B T}$ with ω being the phonon angular frequency and the Debye temperature $\theta_{D,i}$, is associated with the phonon cutoff frequency at the Brillouin zone boundary.

The combined phonon relaxation time (τ_i^C) consists of normal scattering (τ_i^N) and resistive scattering (τ_i^R). Resistive scattering encompasses several mechanisms that impede phonon transport, including phonon-phonon Umklapp scattering (τ_i^U), phonon-point defect scattering (τ_i^P), phonon-boundary scattering (τ_i^B), phonon-dislocation scattering (τ_i^D), etc. Therefore, we have:

$$\frac{1}{\tau_i^C} = \frac{1}{\tau_i^N} + \frac{1}{\tau_i^R} \quad (S5)$$

$$\frac{1}{\tau_i^R} = \frac{1}{\tau_i^U} + \frac{1}{\tau_i^P} + \frac{1}{\tau_i^B} + \frac{1}{\tau_i^D} + \dots \quad (S6)$$

The phonon relaxation times for a specific scattering mechanism are defined as follows:

$$\frac{1}{\tau_i^U} = \frac{\hbar\gamma_i^2}{Mv_i^2\theta_D} \omega^2 T \exp\left(-\frac{\theta_{D,i}}{3T}\right) \quad (S7)$$

$$\frac{1}{\tau_i^B} = \frac{v_i}{L_c} \quad (S8)$$

$$\frac{1}{\tau_i^P} = \frac{V\Gamma}{4\pi v_i^3} \omega^4 \quad (S9)$$

$$\frac{1}{\tau_L^N} = \frac{k_B^3 \gamma_L^2 V}{M\hbar^2 v_L^5} \omega^2 T^3 \quad (S10)$$

$$\frac{1}{\tau_T^N} = \frac{k_B^4 \gamma_T^2 V}{M\hbar^3 v_T^5} \omega T^4 \quad (S11)$$

where γ_i is the Grüneisen constant, M is the average atomic mass of the crystal, V is the volume per atom, L_c is the characteristic dimension of the sample, Γ represents the scattering parameter related to the point defects.

For phonon-dislocation scattering, it consists of contributions from dislocation cores (τ_i^{DC}) and strain fields (τ_i^{DS}).

$$\frac{1}{\tau_i^D} = \frac{1}{\tau_i^{DC}} + \frac{1}{\tau_i^{DS}} \quad (S12)$$

Klemens model³ is used to interpret the interaction between dislocations and phonons.

$$\frac{1}{\tau_i^{DC}} = N_D \frac{V_0^{\frac{4}{3}}}{v_i^2} \omega^3 \quad (S13)$$

$$\frac{1}{\tau_i^{DS}} = 0.06b^2 N_D \gamma_i^2 \omega \quad (S14)$$

where V_0 is the volume of the unit cell, b is the Burgers vector, N_D is the dislocation density.

The phonon scattering rate caused by stacking faults is expressed as^{4,5}:

$$\frac{1}{\tau_i^{SF}} = \frac{0.7a^2 \gamma_i^2 N_S}{v_i} \omega^2 \quad (S15)$$

where N_S is number of stacking faults per unit length. In our case, N_S is estimated based on the dislocation density.⁴

The parameters used for modeling are listed in **Table S1**. The physical properties including v_i , $\theta_{D,i}$ and γ_i are taken from the literature². The Burgers vector is taken from our previous work⁶.

Table S1. The list of parameters used for the modified Debye-Callaway model.

Parameter	Value
k_B	$1.380649 \times 10^{-23} \text{ J K}^{-1}$
\hbar	$1.054571817 \times 10^{-34} \text{ J}\cdot\text{s}$
M	$6.09 \times 10^{-26} \text{ Kg}$
V	$1.19 \times 10^{-29} \text{ m}^3$
V_0	$5.95 \times 10^{-29} \text{ m}^3$
v_L	$8500 \text{ m s}^{-1} \text{ ref. [2]}$
v_T	$5200 \text{ m s}^{-1} \text{ ref. [2]}$
$\theta_{D,L}$	192 K ref. [2]
$\theta_{D,T}$	173 K ref. [2]
γ_L	2.6 ref. [2]
γ_T	0.7 ref. [2]
b	$5.52 \text{ \AA ref. [6]}$
N_D	10^{15} m^{-2}
N_S	$2.5 \times 10^6 \text{ m}^{-1}$

4. Impact of boundary scattering for single-crystal ρ -STO:

It may be argued that boundary scattering is negligible in single-crystal STO due to the absence of grain boundaries. This is the case in the high-temperature regime, but at low temperatures (below $\sim 105 \text{ K}$) domains can form and act as sources for boundary scattering. Here we present the modeling results without and with boundary scattering considered. If we assume the single crystal has no boundaries of any kind, the characteristic length L_c can be considered as the sample thickness, which is 1 mm in this case. Therefore, we set L_c to 1 mm and then fit the point defect scattering parameter Γ . The fitted Γ is 0.4542 , as displayed by the black dash line in **Fig. S3**, although the large discrepancies are observed between the fitted and measured data. Moreover, the fitted Γ of 0.4542 is excessively large, far beyond

realistic expectations, as it is typically less than 0.1, even in entropy-engineered samples with high concentrations of point defects.^{7,8} Then we set Γ to 0.4542 and exclude the boundary scattering. The calculated data (black solid line in **Fig. S3**) is slightly higher than the data with boundary scattering included at low temperatures but converges to the same level above 100 K. This suggests that boundary scattering only significantly affects thermal conductivity at extremely low temperatures when L_c is very large. To visualize the impact of L_c , we then set L_c to 1 μm and fit parameter Γ . As shown by the red dash line in **Fig. S3**, the modeling results with Γ being 0.0452 show smaller discrepancies compared to those with L_c of 1 mm. When boundary scattering is excluded (red solid line in **Fig. S3**), the thermal conductivity increases by a factor of 10 at 50 K, with the differences gradually decreasing as the temperature rises. It suggests that the impact of boundary scattering becomes significant below room temperature when L_c decreases to 1 μm . In short, the trends of the measured thermal conductivity can only be achieved when boundary scattering is considered. By fitting both L_c and Γ , the modeling results align well with the experimental data (see blue dash line in **Fig. S3**). The fitted L_c is 485 nm and Γ is 0.0206, both of which appear reasonable.

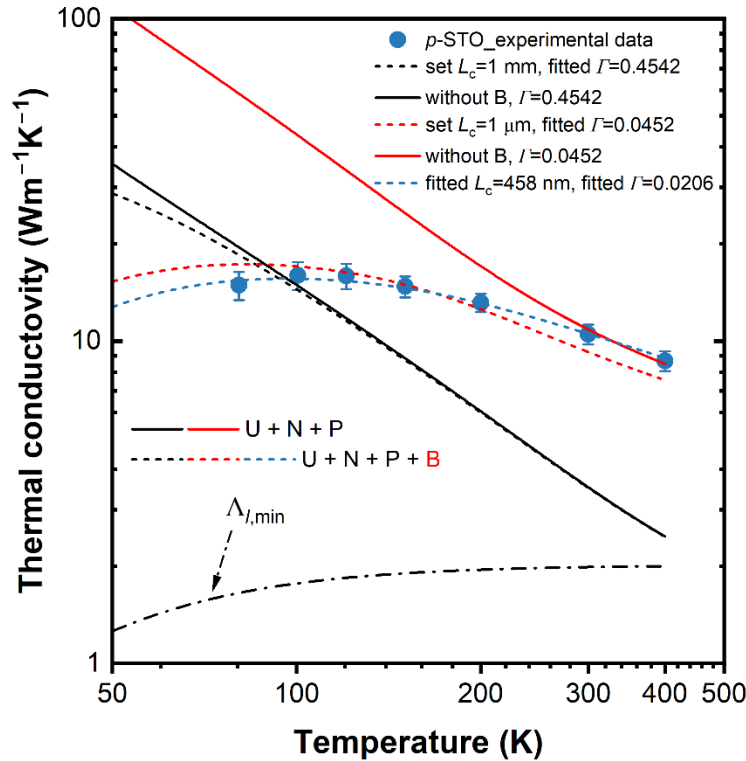


FIG. S3. Modeling analysis of thermal conductivity of p-STO obtained by TDTR method. Note: “U + N + P” includes Umklapp (U) and normal (N) phonon-phonon scattering, along with point defect scattering (P) in the phonon transport process. “U + N + P + B” additionally accounts for boundary scattering (B).

References

- ¹ D.T. Morelli, J.P. Heremans, and G.A. Slack, “Estimation of the isotope effect on the lattice thermal conductivity of group IV and group III-V semiconductors,” *Phys. Rev. B* **66**(19), 195304 (2002).
- ² C. Zhang, F. Liu, S. Guo, Y. Zhang, X. Xu, K.A. Mkhoyan, B. Jalan, and X. Wang, “Temperature-dependent thermal conductivity of MBE-grown epitaxial SrSnO₃ films,” *Appl. Phys. Lett.* **123**(4), 042201 (2023).
- ³ P.G. Klemens, “The Scattering of Low-Frequency Lattice Waves by Static Imperfections,” *Proc. Phys. Soc. Sect. A* **68**(12), 1113–1128 (1955).
- ⁴ M. Khafizov, J. Pakarinen, L. He, and D.H. Hurley, “Impact of irradiation induced dislocation loops on thermal conductivity in ceramics,” *J. Am. Ceram. Soc.* **102**(12), 7533–7542 (2019).
- ⁵ A.J.H. Mante, and J. Volger, “The influence of stacking faults on the thermal conductivity of rutile,” *Physica* **49**(2), 261–277 (1970).
- ⁶ X. Fang, K. Ding, C. Minnert, A. Nakamura, and K. Durst, “Dislocation-based crack initiation and propagation in single-crystal SrTiO₃,” *J. Mater. Sci.* **56**(9), 5479–5492 (2021).
- ⁷ Y. Luo, S. Hao, S. Cai, T.J. Slade, Z.Z. Luo, V.P. Dravid, C. Wolverton, Q. Yan, and M.G. Kanatzidis, “High Thermoelectric Performance in the New Cubic Semiconductor AgSnSbSe₃ by High-Entropy Engineering,” *J. Am. Chem. Soc.* **142**(35), 15187–15198 (2020).
- ⁸ Z. Shi, J. Zhang, J. Wei, X. Hou, S. Cao, S. Tong, S. Liu, X. Li, and Y. Zhang, “A-site deficiency improved the thermoelectric performance of high-entropy perovskite manganite-based ceramics,” *J. Mater. Chem. C* **10**(41), 15582–15592 (2022).